JACS Au
AN OPEN ACCESS JOURNAL OF THE AMERICAN CHEMICAL SOCIETY

Open Access
This article is licensed under CC-BY-NC-ND 4.0

pubs.acs.org/jacsau
Article

Electrolyte Design Chart Reframed by Intermolecular Interactions for High-Performance Li−Ion Batteries

Renzhi Huang, Xin Guo, Binbin Chen, Mengying Ma, Qinlong Chen, Canfu Zhang, Yingchun Liu, Xueqian Kong, Xiulin Fan, Linjun Wang,* Min Ling,* and Huilin Pan*

Cite This: *JACS Au* 2024, 4, 1986−1996

Read Online

ACCESS | Metrics & More | Article Recommendations | Supporting Information

ABSTRACT: Developing advanced electrolytes has been regarded as a pivotal strategy for enhancing the electrochemical performance of batteries; however, the criteria for electrolyte design remain elusive. In this study, we present an electrolyte design chart reframed through intermolecular interactions. By combining systematic nuclear magnetic resonance, Fourier transform infrared measurements, molecular dynamics (MD) simulations, and machine-learning-assisted classifications, we establish semiquantitative correlations between electrolyte components and the electrochemical reversibility of electrolytes. We propose the equivalent increment of Li salt resulting from functional cosolvent and solvent−solvent interactions for effective electrolyte design and prediction. The controllable regulation of the electrolyte design chart by the properties of solvent−solvent interactions presents varying equivalent effects of increasing Li salt concentrations in different electrolyte systems. Based on this mechanism, we demonstrate highly reversible and nonflammable phosphate-based electrolytes for graphite‖NCM811 full cells. The proposed electrolyte design chart, semiquantitatively determined by intermolecular interactions, provides the necessary experimental foundation and basis for the future rapid screening and prediction of electrolytes using machine-learning methods.

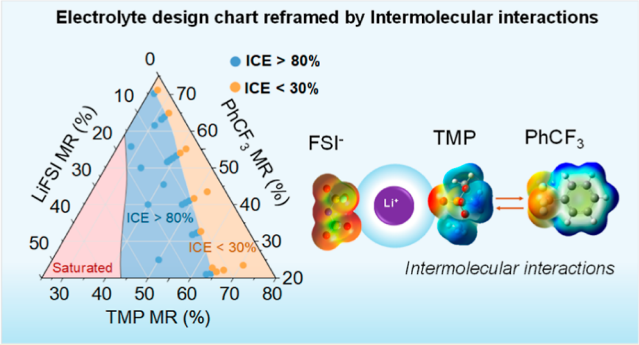

KEYWORDS: *lithium−ion batteries, electrolyte design chart, intermolecular interactions, machine-learning classification*

1. INTRODUCTION

With the rapid growth of electric vehicles and large-scale energy storage, the demand for lithium−ion battery (LIB) products with high energy density and high safety is continuously increasing.[1−3] Traditional carbonate-based electrolytes are inadequate to meet the growing needs of high-performance LIBs. It is prominent to enhance the electrochemical stability of electrolytes while restricting the flammable hazards and enhancing the ionic conductivity with reduced viscosity and cost.[3−7] Unfortunately, it is difficult to balance these features in multifunctional electrolytes for the practical use of batteries. In recent years, researchers have proposed the electrolyte design concepts with high concentrations of salts to expand the electrochemical stability of different types of electrolytes with new solvents.[8−13] Furthermore, localized high-concentration electrolytes have also provided helpful ideas to couple with the electrochemical stability and other properties of electrolytes.[14−17] However, the design of diluted electrolytes still relies on trial and error; controllable modulation of fundamental interactions remains elusive.

Researchers have tried to reveal the regulation of molecular interactions in electrolyte solutions and illustrate the working mechanisms of functional electrolytes. Cao et al. proposed a useful concept of the coordination number rule for designing high-performance electrolytes by regulating the ion−solvent interaction structures.[18−20] Combining low-solvation solvent with the high-solvation solvent in electrolytes was introduced as an effective approach to form a stable local solvation structure with more anion participation and enhanced reduction stability.[21,22] Xie et al. further reported that the local solvation is highly associated with the dielectric constant and geometry of the solvent molecules.[23−26] Besides, it has been reported that the solvent−solvent intermolecular interactions could strongly regulate the local and even long-range structure of electrolytes with modified electrochemical stability and ion transport properties.[27−30]

In a practical complex electrolyte, the competition of strong interactions (i.e., cation−anion and cation−solvent) and weak

Received: March 3, 2024
Revised: April 19, 2024
Accepted: April 24, 2024
Published: May 3, 2024

ACS Publications
© 2024 The Authors. Published by American Chemical Society

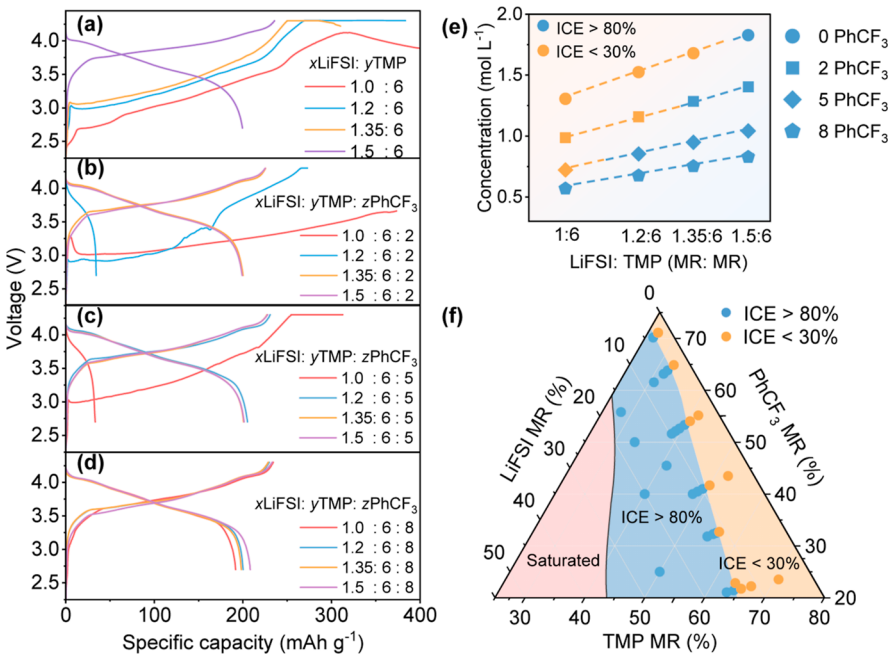

Figure 1. Compatibility of xLiFSI-yTMP-zPhCF$_3$ electrolytes in graphite||NCM811 cells. (a−d) Initial charge−discharge curves of the graphite||NCM811 cells in the electrolytes at xLiFSI/yTMP/zPhCF$_3$ MRs from 1:6:0 to 1.5:6:8. (e) Overall concentration of LiFSI in electrolytes with different proportions. (f) Ternary chart of the MR of electrolyte components in terms of ICEs of graphite||NCM811 cells. In (e,f), the blue data points represent the electrolytes with ICE > 80%, while the orange data points represent irreversible behavior (ICE < 30%).

interactions (i.e., solvent−solvent interaction) plays crucial roles in constructing the structure and electrochemical properties of electrolytes. Recognizing the complete picture of the electrolyte is challenging when only the variation of a single component is controlled. Furthermore, the quantitative correlation and synergy between different interactions and electrolyte performance remain unclear, making it challenging to comprehensively illustrate electrolyte design criteria. In this work, we revealed a ternary chart of electrolyte compositions with regard to the compatibility of the corresponding electrolytes in batteries, which provides a fundamental basis for efficient electrolyte screening. We selected xLiFSI-yTMP-zPhCF$_3$ (LiFSI/lithium bis(fluorosulfonyl)imide, TMP/trimethyl phosphate, and PhCF$_3$/trifluorotoluene) as demonstrative electrolytes and carefully discussed the controllable relationship between solvent structure and battery performance. Coupled with nuclear magnetic resonance (NMR), Fourier transform infrared (FT-IR), molecular dynamics (MD) simulations, and machine-learning-assisted classification methods, it is found that tuning the intermolecular interactions between solvents can be an important approach to reframing the chart for electrolyte design, which can be equivalent to adjusting the Li salt concentration.

2. RESULTS AND DISCUSSION

2.1. Electrolyte Design Chart for Ternary xLiFSI-yTMP-zPhCF$_3$

From binary to ternary electrolyte compositions and beyond, it is crucial to revisit the (semi) quantitative correlations between the molar ratio (MR) of salt to solvation solvent in electrolytes and their impacts on electrochemical compatibility in batteries. Trimethyl phosphate (TMP) is employed as the solvation solvent that exhibits strong interaction with Li$^+$, good oxidation stability, and nonflammability.[31,32] But TMP shows incompatibility toward graphite on the anode side due to an uncontrollable reduction reaction and the cointercalation of TMP solvent.[33] LiFSI is used as the electrolyte salt for the TMP-based electrolyte. PhCF$_3$ that does not dissolve LiFSI is used as the weak cosolvent to tune the solvation interactions via weak solvent−solvent interactions. Graphite||LiNi$_{0.8}$Mn$_{0.1}$Co$_{0.1}$O$_2$ (NCM811) full cells (graphite||NCM811) are employed to evaluate the electrochemical performance of TMP-based electrolytes. The MR of LiFSI/TMP is systematically tuned to track its dynamic correlation to the electrochemical performance of such electrolytes. Initial Coulombic efficiency (ICE) is a useful indicator of the electrochemical compatibility of the electrolytes in cells. In the binary electrolytes of LiFSI-TMP, the reversibility of the graphite||NCM811 cell in the initial cycle is strongly dependent on the MR of LiFSI/TMP, as shown in Figure 1a. As the MR of LiFSI/TMP increases to a critical value of 1.5:6 (1:4), the reversibility of the cell is dramatically enhanced with ICE >80%, which is consistent with previous reports.[20,32] At lower MR of LiFSI/TMP, the cell cannot properly charge due to the side reactions on the graphite anode at ∼1 V vs Li$^+$/Li (illustrated by the three-electrode charge−discharge curves in Figure S1).

After PhCF$_3$ is introduced into the binary LiFSI-TMP electrolytes with different MR, it is found that the reversibility of the full cell exhibits regular changes. As the increasing molar content of PhCF$_3$ in LiFSI-TMP-PhCF$_3$ solution, the critical MR value of LiFSI/TMP (that enables reversible operation of the cell) decreases from 1.5:6 in xLiFSI-yTMP-0PhCF$_3$ to 1.35:6 (xLiFSI-yTMP-2PhCF$_3$), 1.2:6 (xLiFSI-yTMP-5PhCF$_3$), and then 1:6 (xLiFSI-yTMP-8PhCF$_3$), as shown in Figure 1b−d. It is a consensus that increasing the Li salt ratio in xLiFSI-yTMP gradually stabilizes the electrolyte due to the reduced free solvent molecules and the increasing anion involved in the solvation shells.[9,34] The low-solvation PhCF$_3$ shows no dissociation capabilities toward LiFSI, but the critical

https://doi.org/10.1021/jacsau.4c00196
JACS Au 2024, 4, 1986−1996

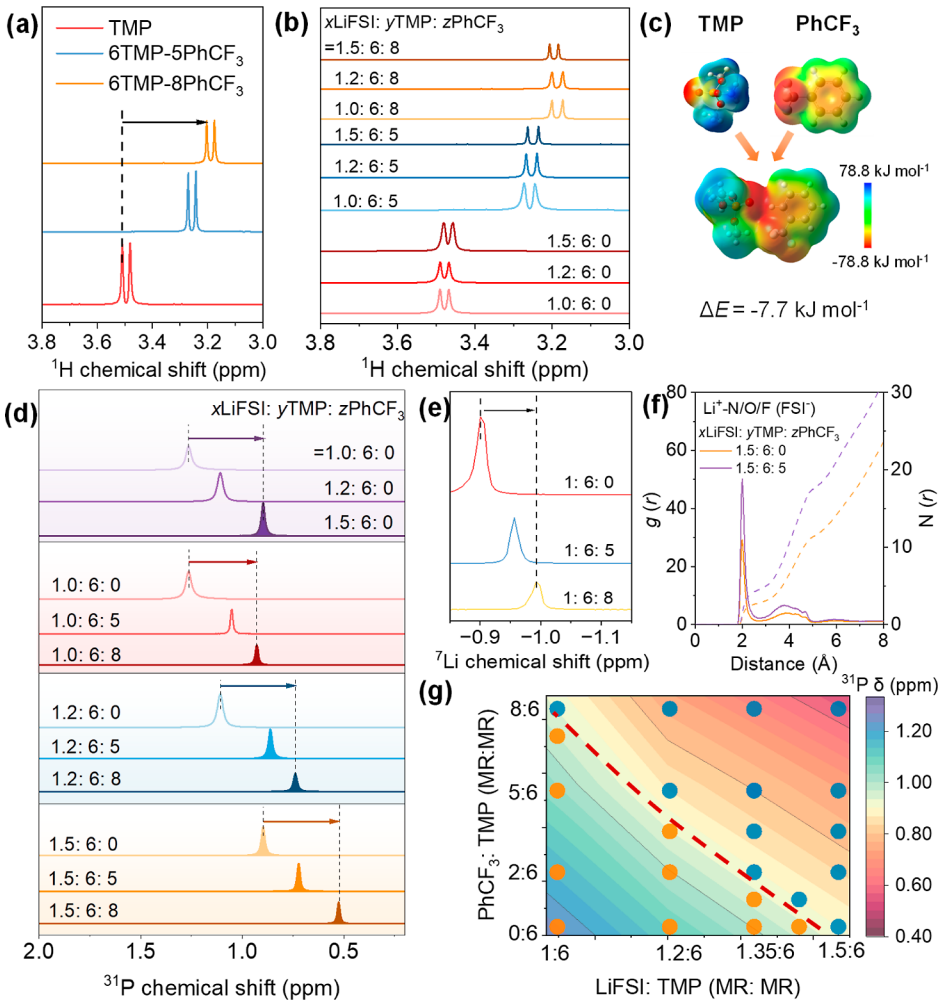

Figure 2. Interactions in the xLiFSI-yTMP-zPhCF$_3$mixtures. (a) ^{1}H NMR spectra for TMP and 6TMP-zPhCF$_3$ solvent mixture (z = 5, 8). (b) ^{1}H NMR spectra for xLiFSI-yTMP-zPhCF$_3$ mixtures, where similar colored lines represent the same TMP-PhCF$_3$ MR. (c) Molecular electrostatic potential (ESP) obtained from DFT calculations of TMP, PhCF$_3$, and TMP-PhCF$_3$. (d) ^{31}P NMR and (e) ^{7}Li NMR results for LiFSI-6TMP-zPhCF$_3$ electrolytes (z = 0, 5, and 8). (f) RDF curves for Li$^+$−N/O/F (FSI$^-$) in 1.5LiFSI-6TMP and 1.5LiFSI-6TMP-5PhCF$_3$ from MD simulations. (g) Contour map of ^{31}P NMR chemical shifts and ICE of graphite||NCM811 cells in xLiFSI-yTMP-zPhCF$_3$ electrolytes. Blue data points represent ICE > 80%, while the orange data points represent ICE < 30%.

MR of salt to solvent (x/y) can obviously decrease for the xLiFSI-yTMP-zPhCF$_3$ mixture electrolytes. Figure 1e summarizes the electrochemical compatibility of different mixture electrolytes in Figure 1a−d based on "MR of LiFSI/TMP". Taking ICE of >80 and <30% as the rough standard for evaluating the compatibility, the overall concentration of LiFSI in the mixture electrolytes can decrease from 1.89 mol L^{-1} (0 PhCF$_3$) to 0.82 mol L^{-1} (8 PhCF$_3$). Interestingly, the compatible and incompatible zones seem to exhibit a clear boundary, as shown in Figure 1e. These results indicate that the low-solvation solvent could play a critical role in regulating the electrochemical stability of electrolytes.

To further unveil the correlation of the fundamental underlying laws controlling the compatibility of electrolytes, we evaluate a series of xLiFSI-yTMP-zPhCF$_3$ electrolytes in Figure 1f, where each data point presents one electrolyte formulation. The ternary chart can be divided into three regions: the red, blue, and orange regions. The red region indicates the saturation of the ternary mixture electrolyte with incomplete salt dissolution or phase separation. The mixture electrolytes in the blue region all exhibit high electrochemical compatibility with ICE > 80%, while the orange region presents the electrolytes with ICE lower than 30%. Surprisingly, a sharp and almost linear boundary can be observed between the blue and orange regions. The electrolytes in the adjacent orange region are unable to store Li reversibly, and the ICE shows a sharp decline compared with the adjacent blue region with close electrolyte ratios (Figure S2). The sharp boundary for the compatibility of electrolytes suggests the existence of a controllable electrolyte design law that might be (semi) quantitatively regulated by a functional cosolvent.

To understand the role of PhCF$_3$ in regulating electrolyte stability, NMR was performed to study the underlying interactions in the mixture of electrolytes. The ^{1}H NMR of CH$_3$ in TMP exhibits an obvious upfield chemical shift in the mixture of solvent with PhCF$_3$ (Figure 2a), which can be attributed to increased shielding of the CH$_3$ group due to intermolecular interactions with PhCF$_3$.[28] Such intermolecular interactions can also be evidenced by the chemical shifts of ^{19}F (CF$_3$ in PhCF$_3$) with the mixing of TMP solvent (Figure S3). In addition, the ^{1}H (TMP) and ^{19}F (PhCF$_3$) NMR peaks can be well retained regardless of the salt concentrations in the ternary mixture electrolytes, as shown in Figures 2b and S4.

https://doi.org/10.1021/jacsau.4c00196
JACS Au 2024, 4, 1986−1996

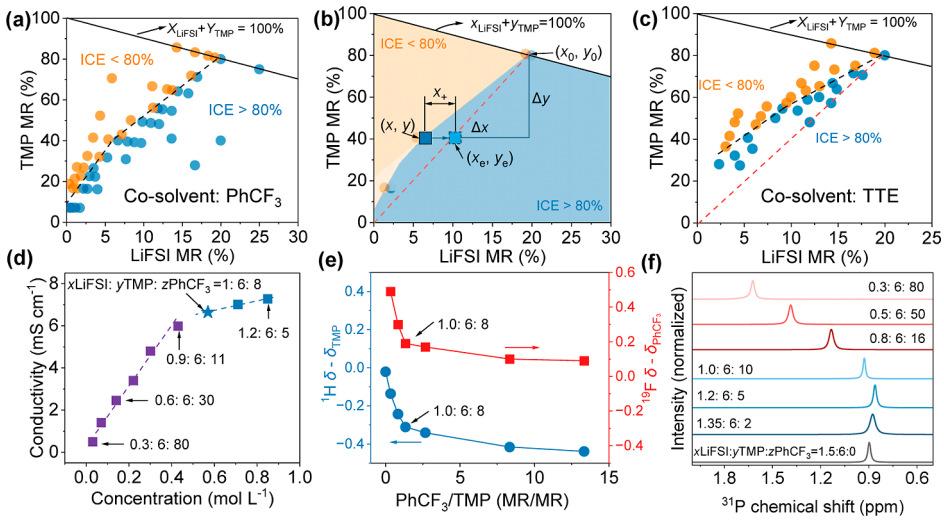

Figure 3. Machine-learning-assisted classification for electrolytes. (a) ICE classification results for different xLiFSI-yTMP-zPhCF$_3$ electrolytes based on a classification criteria of 80%. Dashed line represents the fitted results of the ICE classification, and the solid line represents the electrolyte with a total MR of TMP and LiFSI of 100% (no PhCF$_3$). (b) Schematic for the calculation of the equivalent increment of MR for LiFSI. (c) Classification results for xLiFSI-yTMP-zTTE electrolytes. (d) Conductive results for electrolytes on the hyperplane fitting lines. (e) Relative NMR shifts for ^{1}H (TMP) and ^{19}F (PhCF$_3$) for electrolyte formulations located on the hyperplane fitting line. (f) NMR spectra for ^{31}P (TMP) of xLiFSI-yTMP-zPhCF$_3$ electrolytes on the hyperplanes.

The NMR results indicate that such TMP-PhCF$_3$ solvent−solvent interactions can be a type of integral interaction in electrolytes, and they are seldomly influenced by dissolved salt thus, such interactions cannot be ignored when designing electrolytes.[35,36] Previous work reported that the solvent−solvent interactions could provide a strategy to stabilize the electrolyte via the reorganization of solvent systems with improved stability.[28,37] Density functional theory (DFT) calculations show that the interaction strength between TMP and PhCF$_3$ is −7.9 kJ mol^{-1}, indicating a weak dipole−dipole interaction (δ^+H−δ^-F) in Figure 2c. MD simulations for a large number of mixed solvents show similar results (Figure S5).

It is critical to figure out how the solvent interactions from TMP-PhCF$_3$ influence the main interaction between Li and TMP in a quantitative or semiquantitative manner to unveil the electrolyte design law. The nonbridged P═O bond in TMP is the primary coordination site toward Li$^+$ cations in the electrolytes due to the strong electrostatic interaction.[38] As the MR of LiFSI/TMP in the xLiFSI-yTMP-0PhCF$_3$, the ^{31}P NMR signals upshift from 1.26 ppm in 1LiFSI-6TMP to 0.93 ppm in 1.5LiFSI-6TMP due to the enhanced shielding effect on P nuclei after interacting with more LiFSI salt (Figure 2d). The NMR results indicate a notable positive correlation between the chemical shifts of ^{31}P NMR signals and the MR of LiFSI, which governs the electrochemical performance of the electrolytes, as discussed in Figure 1. The highlighted ^{31}P NMR peak at 0.93 ppm for 1.5LiFSI-6TMP suggests a critical MR value that enables the reversibility of graphite||NCM811 full cells. A gradual upfield of ^{7}Li NMR signal can also be correspondingly observed with increasing MR of LiFSI/TMP due to the enhanced interaction between Li$^+$ and FSI$^-$ anion and TMP solvent (Figure S6), which is consistent with previous reports in concentrated electrolytes.[39,40]

As introducing PhCF$_3$ in the xLiFSI-yTMP-zPhCF$_3$ mixture electrolytes, the ^{31}P NMR peaks shift to the highlighted peak position of ∼0.93 ppm in advance under lower MR of LiFSI/TMP, such as 1:6 and 1.2:6, as shown in the red and blue panels of Figure 2d. The decrease in critical MR that enables the reversible operation of the cells highly depends on the molar amount of PhCF$_3$ in the ternary mixture. Besides, the ^{7}Li NMR peaks continue to shift toward the upfield direction by introducing more PhCF$_3$ at the same MR of LiFSI/TMP, which originally required a larger Li salt MR (Figure 2e). In other words, PhCF$_3$ presents an analogy effect of increasing LiFSI MR when tuning the solvent structure of Li$^+$ in the ternary electrolytes. PhCF$_3$ does not participate in the internal solvation sheath of Li$^+$ (indicated by the radial distribution function (RDF) of Li−PhCF$_3$, Figure S7); therefore, it indirectly influences the solvation structure of Li$^+$ by interacting with TMP. RDF of Li−N/O/F(FSI$^-$) obtained from MD simulation also suggests that PhCF$_3$ leads to enhanced coordination of the FSI$^-$ anion with the Li$^+$ cation via the solvent interactions (TMP-PhCF$_3$) (Figure 2f). The proportion of FSI$^-$ and TMP in the first solvation shell derived from the MD simulation shows that the coordination proportion of FSI$^-$ increases while the proportion of TMP decreases in the ternary electrolytes (Figure S8). Raman analysis of the P═O state of TMP shows a slight increase in free TMP molecules as PhCF$_3$ increases (Figure S9), indicating that the weak cosolvent of PhCF$_3$ pulls the solvating TMP out of the coordination shell of Li$^+$, which is further stabilized by the solvent interactions.[25,26] The regulated solvation structure of Li$^+$ via weak solvent−solvent interactions would weaken the local solvation strength and be beneficial for Li$^+$ transport and deassociation, which could be beneficial to enhance the interfacial reaction kinetics in batteries.

To explore the (semi) quantitative relationship between electrolyte properties and cell performance, a contour map of chemical shifts of ^{31}P for different xLiFSI-yTMP-zPhCF$_3$ mixtures was based on the MR of LiFSI/TMP (x-axis) and PhCF$_3$/TMP (y-axis), as shown in Figure 2g. This contour map is based on the observed positive correlation between the chemical shift of the ^{31}P NMR and the MR of Li salt. The scatter plots of ICE from graphite||NCM811 cells in different mixture electrolytes are also listed in Figure 2g. Blue dots

https://doi.org/10.1021/jacsau.4c00196
JACS Au 2024, 4, 1986−1996

indicate ICE >80% and red dots indicate ICE <30%. The demarcation line between the reversible and irreversible regions surprisingly coincides with a ^{31}P NMR shift at ∼0.95 ppm (that enables the stable operation of xLiFSI-yTMP in the binary electrolytes). This indicates a strong and controllable correlation between the electrolyte solvation environment and the electrochemical performance of cells. It is reasonable to speculate on a mixture electrolyte of xLiFSI-yTMP-zPhCF$_3$ that exhibits ^{31}P NMR shift at ∼0.95 ppm and lower ppm can enable reversible Li storage for the graphite‖NCM811 cells.

To further prove the correlation between solvation and cell performance with xLiFSI-yTMP-zPhCF$_3$ electrolytes, a series of FT-IR measurements were performed to characterize the evolution of solvation structures via monitoring the coordination status of FSI$^-$ anions in Figures S10 and S11. FSI$^-$ anions in the xLiFSI-yTMP-zPhCF$_3$ electrolytes basically demonstrate the solvent-separated ion pairs (SSIP), contact ion pairs (CIP), and aggregates (AGG) coordination status of FSI$^-$ anions (Figure S10). Figure S11 demonstrates the contour maps of proportions of CIP, AGG, and CIP + AGG based on the MR of LiFSI/TMP (x-axis) and PhCF$_3$/TMP (y-axis) in the mixture electrolytes. The scatter plots of ICE for different electrolytes are also placed in Figure S11 to determine the underlying interactions and correlations. It is found that the counter maps of AGG show the highest correlation between the solvation structures of the electrolyte and the electrochemical compatibility of the electrolyte in a cell. The proportion of AGG≥ ∼ 13% is a critical criterion of solvation structures that enable relevant reversibility of the cells. Thus, we have established a semiquantitative connection between the first-cycle performance of the graphite‖NCM811 cells and the solvation structure of mixture electrolytes, which is intensively regulated by the interaction of PhCF$_3$-TMP.

2.2. Machine-Learning Classification for Ternary Electrolytes

As discussed above, ICE is a simple and effective indicator to exhibit the electrochemical stability of electrolytes in cells when designing electrolytes. We further employed a machine-learning classification approach to sort the mixture for xLiFSI-yTMP-zPhCF$_3$ electrolytes based on the variable ICE with a criterion of 80%. The classification results show that the boundary distinguishing reversible and irreversible electrolytes has a significant two-segment linear pattern (Figure 3a). Detailed ICEs can be found in Table S1 of the Supporting Information. Within the overall MR range of 5−20% for LiFSI and 40−80% for TMP (corresponding to a regular Li salt concentration of 0.57−1.89 mol L^{-1}), if a single linear function was used to fit the data points, we obtained the following relation

$$y_{\mathrm{TMP}} = 3.03x_{\mathrm{LiFSI}} + 0.22 \tag{1}$$

Below such hyperplane, all xLiFSI-yTMP-zPhCF$_3$ electrolyte data points exhibit ICE >80% in graphite‖NCM811 cells. To understand the potential physical meaning of the slope for the hyperplane (denoted by c_1, c_1 = 3.03), Figure 3b illustrates some special lines and data points for the classification results. Point (x_0, y_0) represents the electrolyte of 1.5LiFSI-6TMP-0PhCF$_3$ with a critical TMP/LiFSI MR of 4 (y_0/x_0 = 4). The red dashed line marks all positions where TMP/LiFSI = 4, and thus all workable electrolytes above the red dashed line are with TMP/LiFSI >4. NMR analysis in Figure 2d indicates that the ^{31}P NMR peak in the electrolyte along the boundary (y/x > 4 in xLiFSI-yTMP-zPhCF$_3$) is equivalent to the ^{31}P NMR peak in the 1.5TMP-6LiFSI (y/x = 4) without PhCF$_3$. Therefore, PhCF$_3$ in the ternary xLiFSI-yTMP-zPhCF$_3$ electrolytes presents an effect of increasing the effective MR of LiFSI salt. Once the equivalent increase in LiFSI salt reaches the red dashed line (y/x = 4), the electrolyte can start to allow a reversible reaction. To identify the semiquantitative role of PhCF$_3$ in xLiFSI-yTMP-zPhCF$_3$ electrolytes, we define an equivalent increment of Li salt MR x_+ for the electrolytes located on (or near) the linear hyperplane in Figure 3b (see details in Supporting Information)

$$x_+ = \frac{c_0 - c_1}{c_0}(x_0 - x) \tag{2}$$

Here, c_0 represents the critical MR for TMP/LiFSI without PhCF$_3$ (c_0 = 4 in this work), which is determined by the properties of LiFSI and TMP. As indicated in Figure 3b, the point (x, y) on the linear boundary, when translated by x_+, reaches the point (x_e, y_e) located on the red dashed line with the equation $y = 4x$. Fundamentally, this effective augmentation of x_+ for LiFSI is a result of cosolvent PhCF$_3$ and its interactions with TMP in xLiFSI-yTMP-zPhCF$_3$ mixture electrolytes, as discussed above in Figure 2. Based on the relationship of $x + y + z = 1$, we further transform eq 2 into a relationship between x_+ and the MR of PhCF$_3$ represented by z (see details in Supporting Information)

$$x_+ = \frac{c_0 - c_1}{c_0(c_1 + 1)}z \tag{3}$$

$$x_+ = 0.0602z(\text{for co} - \text{solvent of PhCF}_3)$$

The relationship between x_+ and the PhCF$_3$ MR z shows a linear correlation, indicating that a higher MR of PhCF$_3$ in the mixture electrolyte could lead to a greater increase in the equivalent increment of Li salt MR.

To validate the concept of an equivalent increment for Li salts, we calculated x_+ for the data points above the linear plane. Choosing a data point with the ratio of xLiFSI/yTMP/zPhCF$_3$ = 1.0:6:5 (equivalent to 0.083:0.5:0.4166), the calculated value of x_+ is 0.0251. Therefore, the equivalent LiFSI MR (x_e) is calculated as $x_e = x + x_+ = 0.083 + 0.0251 = 0.1081$, and $y/x_e = 4.63$, still greater than 4. Consequently, the mixture electrolyte with this MR still fails to meet the required conditions. This was confirmed by practical electrochemical measurement, namely, this electrolyte cannot support the reversible operation of graphite‖NCM811 cells. These results indicate that the proposed equivalent MR of Li salts and the equivalent increment of x_+ (due to solvent effects) can effectively predict the reversibility of the electrolyte in the batteries.

Once the relationship between the MRs in electrolyte and electrochemical performance is established, it becomes imperative to guide a judicious selection of the electrolyte components and compositions and thus efficiently enhance battery performance with reduced cost. We further evaluate a different type of cosolvent 1,1,2,2−tetrafluoroethyl−2,2,3,3−tetrafluoropropylether (TTE) in xLiFSI-yTMP-zTTE electrolyte systems. Figure S12 shows the ICE of graphite‖NCM811 cells in different xLiFSI-yTMP-zTTE electrolytes. Figure 3c exhibits the classification results for the reversibility of xLiFSI-yTMP-zTTE electrolytes in plots similar to those in Figure 3a. A similar linear boundary that separates the reversible and

https://doi.org/10.1021/jacsau.4c00196
JACS Au 2024, 4, 1986−1996

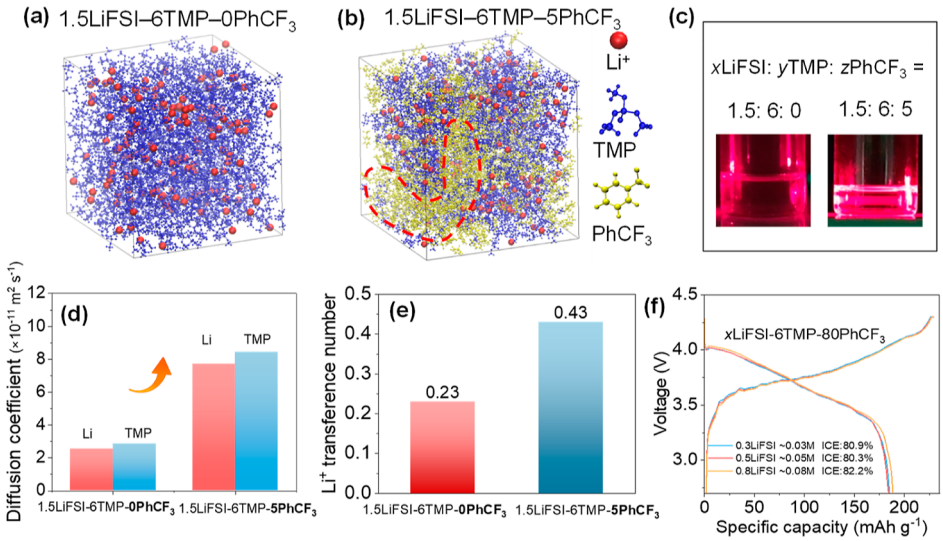

Figure 4. MD simulations and transport properties for LiFSI-TMP-$PhCF_3$electrolytes. (a,b) Snapshots of MD simulations for xLiFSI/yTMP/$z$$PhCF_3$ = 1.5:6:0 and 1.5:6:5 electrolytes, respectively. Red dashed circle marks the $PhCF_3$ cluster. (c) Tyndall effect test results of 1.5:6:0 and 1.5:6:5 electrolytes. (d) Diffusion coefficients in 1.5:6:0 and 1.5:6:5 electrolytes. Diffusion coefficients were derived from the PFG-NMR results for electrolytes (Figure S16). (e) Li^+ transference number for 1.5:6:0 and 1.5:6:5 electrolytes. (f) Initial charge−discharge curves for graphite‖NCM811 cells using ultradilute electrolyte xLiFSI-6TMP-80$PhCF_3$ (x = 0.3, 0.5, and 0.8).

irreversible zones is presented in a certain range. The boundary is linearly fitted as follows

$$y_{TMP} = 2.42x_{LiFSI} + 0.33 \quad (4)$$

$$x_{+} = 0.115z(\text{for co} - \text{solvent of TTE})$$

The factor in front of z as c_1 = 2.42 for TTE is smaller than c_1 = 3.03 for $PhCF_3$, indicating that TTE can provide a larger equivalent increase for MR of LiFSI salt in mixture electrolytes. As discussed earlier, the equivalent increase for LiFSI results from solvent−solvent interactions, which extract polar solvent while simultaneously enhancing the coordination of FSI^- anions. This is tantamount to an augmented salt concentration, and the equivalent increase can be precisely quantified. A future combination of machine learning to screen and compare the solvent−solvent interactions can potentially provide effective approaches to reframe the electrolyte charts and guide the electrolyte design.

In addition, it is also found that when significantly increase the $PhCF_3$ in the xLiFSI-yTMP-$z$$PhCF_3$ mixture electrolyte, the hyperplanes that separate the reversible and irreversible electrolytes are obviously changed, as shown in Figure 3a in the MR range of 0−5% for LiFSI, 5−20% for TMP, and 75−95% for the nonsolvating $PhCF_3$. The change of hyperplanes can be due to the obvious evolution of electrolyte structure as the nonsolvating solvent takes up a critical amount of volume/MR in a mixture electrolyte solution. To gain insight into the electrolyte design criteria, we further performed ionic conductivity tests for the data points located on the two-segment boundaries, as shown in Figure 3a. It can be found that the ionic conductivity of electrolytes follows a similar evolution trend. The conductivity on both sides of the intersection of the two-phase boundaries (xLiFSI/yTMP/$z$$PhCF_3$ = 1.0:6:8) exhibits significantly different variation trends (Figure 3d). On the right side of the intersection, with a moderate MR of $PhCF_3$ to the main solvent TMP, the conductivity changes slowly as the LiFSI concentration increases (6−8 mS cm^{-1}). On the left side of the intersection point, $PhCF_3$ gradually becomes the major solvent, where the conductivity changes dramatically with the LiFSI concentration. This indicates significant differences in the solution structure and, thus, the transport mechanism of the electrolyte on both sides of the intersection points. We further conducted NMR studies for the data points located on boundaries to understand the evolution of solvent−solvent interactions in tailoring the electrolyte design criteria. When $PhCF_3$/TMP <1.3, both ^1H (TMP) and ^{19}F ($PhCF_3$) NMR spectra show significant changes with increasing $PhCF_3$ solvent MR, indicating significant TMP-$PhCF_3$ interactions (Figures 3e and S13). However, when $PhCF_3$/TMP >1.3, the change for ^1H and ^{19}F NMR peaks becomes slower or stable, indicating saturation of TMP-$PhCF_3$ interactions in this region (due to the presence of extra $PhCF_3$). The ^{31}P (TMP) NMR spectra in Figure 3f exhibit the significant impact of TMP-$PhCF_3$ solvent−solvent interactions on the evolution of TMP−Li interactions in electrolytes. The ^{31}P NMR peak position of the electrolyte components on the right side of the intersection point remains stable at ca. 0.95 ppm, consistent with the results in Figure 2g. On the other hand, ^{31}P (TMP) NMR peaks exhibit a rapid shift toward the free TMP, which is in line with the increase of coordination by FSI^- anion in this region (Figure S14). The ionic conductivity and NMR results clearly indicate that the electrolyte screening rules can hardly be a unified picture due to the evolution of the microstructure of electrolytes when tuning one or more components in the electrolyte.

2.3. MD Simulations and Transport Properties for Ternary Electrolytes

MD simulations are performed for binary and ternary electrolytes of LiFSI-TMP and LiFSI-TMP-$PhCF_3$ to further understand the difference in electrolyte structures (Figure 4a,b). The MD results suggest that the binary electrolyte exhibits basically a uniform distribution of the electrolyte components (Figure 4a). In comparison, introducing the functional weak cosolvent of $PhCF_3$ generates nanoscale (1−2 nm) heterogeneity in the electrolyte through the sponta-

https://doi.org/10.1021/jacsau.4c00196
JACS Au 2024, 4, 1986−1996

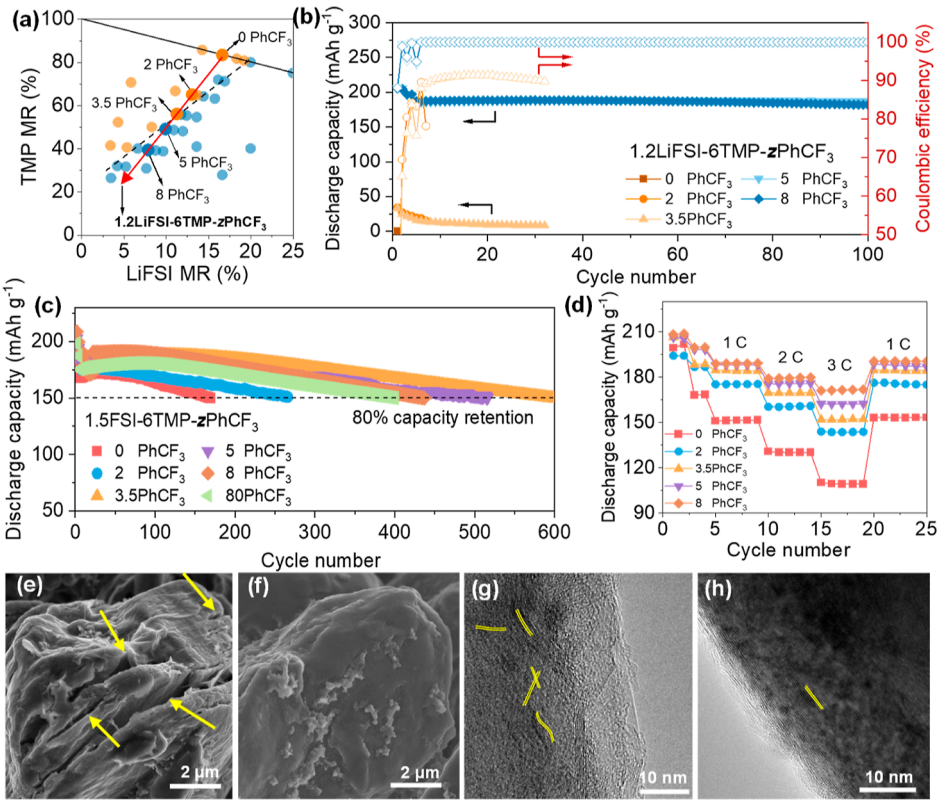

Figure 5. Cycling performance of LiFSI-TMP-$PhCF_3$electrolytes and interfacial properties of graphite anodes. (a) Schematic representation of the position of 1.2FSI-6TMP-based electrolytes with different $PhCF_3$ in the electrolyte chart. Black dashed line is the boundary for the compatibility of electrolytes, and the red arrow across the boundary represents the 1.2LiFSI-6TMP-zPhCF$_3$ with increasing $PhCF_3$ MR. (b) Cycling performance of graphite||NCM811 cells in the 1.2FSI-6TMP-zPhCF$_3$ electrolytes. (c) Cycling performance and (d) rate performance of 1.5LiFSI-6TMP electrolytes with different MR of $PhCF_3$. (e−h) Morphology and structure characterization of graphite anodes after charge and discharge. SEM images of the graphite electrodes cycled at 0.1C with (e) 1.2LiFSI-6TMP-0PhCF$_3$ and (f) 1.2LiFSI-6TMP-5PhCF$_3$ electrolytes in graphite|| NCM811 cells. HRTEM images of the graphite electrodes cycled at 0.1C with (g) 1.2LiFSI-6TMP-0PhCF$_3$ and (h) 1.2LiFSI-6TMP-5PhCF$_3$ electrolytes in graphite||NCM811 cells.

neously formed solvent clusters for $PhCF_3$, which presents the fastest and dynamic transport feature in a mixture electrolyte (Figure S15). Additionally, in the ternary system, we observe an apparent Tyndall effect, which does not exist in the binary system (Figure 4c).

The evolution of MRs of $PhCF_3$ in the ternary mixture electrolyte can greatly reform the electrochemical stability and charge transport mechanism. The rapid migration of $PhCF_3$ solvent clusters may significantly promote the migration of TMP and Li^+, which are adjacent to $PhCF_3$ through $PhCF_3$-TMP interactions. This enhancement can be evidenced by the results of the PFG-NMR experiments: the diffusion coefficients of Li^+ and TMP in the ternary electrolyte are significantly improved by ca. 4 times compared with those in the traditional phosphate-based electrolyte without $PhCF_3$ (Figure 4d, see details in Figure S16a−c). This is also evidenced by the greatly improved ionic conductivity of LiFSI-TMP-$PhCF_3$ ternary electrolytes than the conventional LiFSI-TMP binary electrolyte in a various temperature range (Figure S16d). The enhanced Li^+ diffusion seems somewhat like the ion diffusion promoted by the movement of polymer segments in polymer electrolytes, but the difference is that the transport of "polymer clusters" in the LiFSI-TMP-$PhCF_3$ ternary electrolyte is very rapid. As shown in Figure 4e, this ion diffusion mechanism also significantly increases the transference number of Li^+ (see details in Figure S17). Imagine if the weak cosolvent $PhCF_3$ occupies the overwhelmingly dominant volume fraction in the electrolyte, these clusters of $PhCF_3$ could lead to a cluster network with a topological structure. TMP and Li salt interact with this network, ensuring good electrochemical stability (Figure S18) and certain diffusion characteristics, even at very low salt concentrations. As shown in Figure 4f, the Li salt concentrations in the electrolytes xLiFSI/yTMP/zPhCF$_3$ = 0.3:6:80, 0.5:6:80, and 0.8:6:80 are only 0.03, 0.05, and 0.08 M, respectively, but they still ensure excellent reversibility in the full cell.

2.4. Electrochemical Performances of Ternary Electrolytes

The solvation structure regulated by $PhCF_3$ can not only enhance the ICE of graphite||NCM811 cells but also enable stable operation in subsequent cycles. The 1.2LiFSI-6TMP-zPhCF$_3$ and 1.5LiFSI-6TMP-zPhCF$_3$ electrolytes are used to demonstrate the cycling stability of cells with varying $PhCF_3$ content, considering both electrochemical stability and salt cost, which also exhibit excellent flame-retardant performance (Figure S19). Figure 5a represents the chart of these electrolytes with different z values with regard to their ICE evaluation in graphite||NCM811 cells. The black dashed line is the boundary for the compatibility of electrolytes; the red arrow across the boundary represents the 1.2LiFSI-6TMP-based electrolytes with increasing $PhCF_3$ MR. The cycling performance of 1.2LiFSI-6TMP-zPhCF$_3$ (z = 0, 2, 3.5, 5, and 8) electrolytes is shown in Figure 5b. When the $PhCF_3$ molar content does not reach the critical value of z = 5, the

https://doi.org/10.1021/jacsau.4c00196
JACS Au 2024, 4, 1986−1996

electrolyte cannot enable reversible reactions of graphite‖NCM811 cells, showing limited reversible capacity and low Coulombic efficiency <90% (Figure 5b). Once the z value exceeds 5 in the 1.2LiFSI-6TMP-zPhCF$_3$, the graphite‖NCM811 cells deliver high reversible capacities of 205.0, 196.9, and 187.2 mAh g^{-1} at C/10, C/3, and 1C rates. Excellent cycling stability can be achieved for 1.2LiFSI-6TMP-5PhCF$_3$ and 1.2LiFSI-6TMP-8PhCF$_3$ electrolytes at 1C, showing capacity retention of 97.2% over 100 cycles, and average Coulombic efficiency of 99.98%, as shown in Figure 5b.

Slightly increasing the MR of LiFSI/TMP in the xLiFSI-yTMP-zPhCF$_3$ to 1.5:6 can further enhance the long-term cycling stability of graphite‖NCM811 cells (Figure 5c). Among them, 1.5LiFSI-6TMP-3.5PhCF$_3$ exhibits the best cycling stability and reversible capacity, with 80% capacity retention over 600 cycles. Interestingly, the 1.5LiFSI-6TMP-80PhCF$_3$ electrolyte with a large amount of PhCF$_3$ and an overall LiFSI concentration of ∼0.14 M can still support the graphite‖NCM811 cell for an attractive cycling life over 400 cycles, as shown in Figures 5c and S20. A large amount of PhCF$_3$ in the LiFSI-TMP-PhCF$_3$ mixture does not significantly decrease the conductivity (Figure S21, the conductivity of the 1.5LiFSI-6TMP-80PhCF$_3$ electrolyte remains at 2.15 mS cm^{-1}), supporting the long cycling of the battery and demonstrating that a large amount of PhCF$_3$ does not interrupt the transport pathway of Li$^+$. The concentrated and diluted electrolytes with nonsolvation or weak solvation electrolytes usually restrict the rate performance of full cells due to the sluggish charge transport kinetics in such electrolytes.[41,42] In contrast, thanks to the special role of PhCF$_3$ in tailoring the electrolyte structure and promoting the transport kinetics of Li$^+$, graphite‖NCM811 full cells using 1.5LiFSI-6TMP-zPhCF$_3$ (z = 0, 2, 3.5, 5, and 8) demonstrate greatly improved rate performance than the conventional phosphate-based electrolyte (Figure 5d). It can be found that the concentrated 1.5LiFSI-6TMP electrolyte can deliver a reversible capacity of 199.4 mAh g^{-1} at 0.1C and the reversible capacity quickly decreases at a higher rate, with a capacity of 110.1 mAh g^{-1} at a 3C rate. After introducing PhCF$_3$, the rate performance can be gradually enhanced from z = 2 to 8, with reversible capacities of 143.8, 152.0, 162.3, and 170.8 mAh g^{-1} at 3C rate, respectively.

The interfacial chemistry and stability of the TMP-based ternary electrolyte are further investigated. The TMP-based electrolytes typically show good oxidation stability toward cathodes but exhibit limitations on the anode sides due to poor reduction stability. Therefore, we focus on the interfacial properties of graphite anodes in graphite‖NCM811 full cells. Figure 5e,f shows scanning electron microscope (SEM) images of the graphite electrode after the initial cycle in the electrolytes of 1.2LiFSI-6TMP-0PhCF$_3$ and reversible 1.2LiFSI-6TMP-5PhCF$_3$, respectively. The initial charge−discharge curves are shown in Figure S22. SEM images in Figures 5e and S23 show that the graphite anode with 1.2LiFSI-6TMP-0PhCF$_3$ electrolytes undergoes severe side reactions, resulting in obvious cracking exfoliation. By contrast, when the electrolyte is regulated to the stable region by PhCF$_3$, the graphite anode with 1.2LiFSI-6TMP-5PhCF$_3$ electrolyte exhibits highly reversible Li$^+$ storage while retaining a smooth surface and no change in the morphology of the graphite anode, as shown in Figure 5f. Besides, the graphite anodes can also retain their original morphology after long cycles in xLiFSI-6TMP-80PhCF$_3$ (x = 0.3, 0.5, and 0.8) electrolytes, even with very low Li salt concentrations (Figure S24). High-resolution transmission electron microscopy (HRTEM) characterization further reveals that the graphite anodes in 1.2LiFSI-6TMP-0PhCF$_3$ electrolytes exhibit thick interface layers, disordered and curved graphite layers at the atomic level, possibly due to the solvent cointercalation and accumulation of interfacial side reactions (Figure 5g, compared with the pristine graphite anode in Figure S25). The graphite anodes in the 1.2LiFSI-6TMP-5PhCF$_3$ electrolytes retain well-defined graphite layers and show a thin surface layer, which could be due to the formation of helpful SEI layers on graphite anodes. Energy−dispersive spectroscopy (EDS) mapping and X-ray photoelectron spectroscopy (XPS) measurements confirm the greatly reduced side reactions on graphite anodes (Figures S26 and S27) after introducing appropriate PhCF$_3$ into the mixture electrolyte.

3. CONCLUSIONS

In summary, we have proposed concepts of the equivalent MR of Li salts and the equivalent increment x_+ in ternary electrolytes and demonstrated the electrolyte design chart, which is reframed by intermolecular interactions. The electrolyte design chart can be used to summarize and predict the electrochemical performance of cells. The distinct linear boundary in the design chart indicates a semiquantitatively controllable electrolyte design criterion. Through systematic research on the relationship between electrolyte performance and interactions in mixture electrolytes, we have revealed the intrinsic fundamental factors reframing the design chart. The cosolvent, PhCF$_3$, demonstrates an analogous effect of increasing the LiFSI MR when tuning the solution structure of Li$^+$ in the ternary electrolytes by dipole−dipole interactions, thus successfully regulating battery performance. The machine classification method has assisted in further semiquantitatively studying the electrolyte components that play a regulatory role in the electrolyte design chart, as well as their associated interactions. In the future, one can further consider how to obtain valuable data through simple pre-experiments or calculations for electrolyte design parameters, such as the chemical shift of the solvating solvent that is positively correlated with the effective MR of Li salts. By combining machine learning and classification methods, it will be possible to explore the design charts of different electrolyte systems, accelerating the pace of electrolyte development and promoting the advancement and application of battery technology.

■ ASSOCIATED CONTENT

Supporting Information

The Supporting Information is available free of charge at https://pubs.acs.org/doi/10.1021/jacsau.4c00196.

Detailed methods for electrolyte and electrode preparation; electrochemical and material characterizations; MD and DFT simulation calculations methods; partial charge−discharge curves of the batteries, NMR, FTIR, and Raman spectra for different solvents and electrolytes; detailed data for transference number, conductivity, and diffusion coefficient properties testing; SEM images of graphite anodes, EDS analysis, and XPS results; and ICE data for different batteries and solvent interaction values from MD calculations (PDF)

https://doi.org/10.1021/jacsau.4c00196
JACS Au 2024, 4, 1986−1996

AUTHOR INFORMATION

Corresponding Authors

Linjun Wang − *Department of Chemistry, Zhejiang University, Hangzhou 310012, China; Key Laboratory of Excited-State Materials of Zhejiang Province, Department of Chemistry, Zhejiang University, Hangzhou 310058, China;* orcid.org/0000-0002-6169-7687; Email: ljwang@zju.edu.cn

Min Ling − *Zhejiang Provincial Key Laboratory of Advanced Chemical Engineering Manufacture Technology, College of Chemical and Biological Engineering, Zhejiang University, Hangzhou 310027, China;* orcid.org/0000-0001-6727-9585; Email: minling@zju.edu.cn

Huilin Pan − *Department of Chemistry, Zhejiang University, Hangzhou 310012, China; State Key Laboratory of Clean Energy Utilization, Zhejiang University, Hangzhou 310012, China;* orcid.org/0000-0001-7991-1015; Email: panhuilin@zju.edu.cn

Authors

Renzhi Huang − *Department of Chemistry, Zhejiang University, Hangzhou 310012, China; Zhejiang Provincial Key Laboratory of Advanced Chemical Engineering Manufacture Technology, College of Chemical and Biological Engineering, Zhejiang University, Hangzhou 310027, China*

Xin Guo − *Department of Chemistry, Zhejiang University, Hangzhou 310012, China; Key Laboratory of Excited-State Materials of Zhejiang Province, Department of Chemistry, Zhejiang University, Hangzhou 310058, China*

Binbin Chen − *Department of Chemistry, Zhejiang University, Hangzhou 310012, China;* orcid.org/0000-0002-3910-0426

Mengying Ma − *Department of Chemistry, Zhejiang University, Hangzhou 310012, China*

Qinlong Chen − *Department of Chemistry, Zhejiang University, Hangzhou 310012, China;* orcid.org/0000-0002-4218-2055

Canfu Zhang − *Department of Chemistry, Zhejiang University, Hangzhou 310012, China*

Yingchun Liu − *Department of Chemistry, Zhejiang University, Hangzhou 310012, China;* orcid.org/0000-0003-2392-9114

Xueqian Kong − *Department of Chemistry, Zhejiang University, Hangzhou 310012, China; Institute of Translational Medicine, Shanghai Jiao Tong University, Shanghai 200240, China;* orcid.org/0000-0002-1901-9073

Xiulin Fan − *State Key Laboratory of Silicon and Advanced Semiconductor Materials, School of Materials Science and Engineering, Zhejiang University, Hangzhou 310058, China;* orcid.org/0000-0001-7294-480X

Complete contact information is available at: https://pubs.acs.org/10.1021/jacsau.4c00196

Author Contributions

R.H. and X.G. authors contributed equally. H.P., R.H., and M.L. conceived the concept and designed the experiments. B.C. and Y.C. conducted the MD and DFT calculations. R.H. conducted the experiments and analysis. Under the supervision of L.W., X.G. performed the machine-learning calculations and analysis. C.Q. and X.Q. performed PFG-NMR and analysis. R.H. and H.P. wrote the manuscript. All authors contributed to the discussion and revision of this work. CRediT: **Renzhi Huang** conceptualization, data curation, formal analysis, writing-original draft, writing-review & editing; **Xin Guo** formal analysis, writing-original draft, writing-review & editing; **Binbin Chen** data curation, writing-original draft, writing-review & editing; **Mengying Ma** conceptualization, writing-review & editing; **Qinlong Chen** data curation, writing-original draft, writing-review & editing; **Canfu Zhang** writing-review & editing; **Yingchun Liu** writing-review & editing; **Xueqian Kong** writing-review & editing; **Xiulin Fan** writing-review & editing; **Linjun Wang** supervision, writing-review & editing; **Min Ling** supervision, writing-review & editing; **Huilin Pan** conceptualization, formal analysis, supervision, writing-original draft, writing-review & editing.

Notes

The authors declare no competing financial interest.

ACKNOWLEDGMENTS

This work was supported by the National Natural Science Foundation of China (grant nos. U21A2075 and 22278351) and the Zhejiang Provincial Natural Science Foundation of China (grant no. LR23B030003). L.W. acknowledges the support from the National Natural Science Foundation of China (grant nos. 22273082 and 21922305) and the High Performance Computing Center in Department of Chemistry, Zhejiang University. HRTEM, NMR, Raman, and SEM measurements were performed at the Chemistry Instrument Center Department of Chemistry, Zhejiang University.

REFERENCES

(1) Li, M.; Wang, C.; Chen, Z.; Xu, K.; Lu, J. New concepts in electrolytes. *Chem. Rev.* **2020**, *120*, 6783−6819.

(2) Nan, B.; Chen, L.; Rodrigo, N. D.; Borodin, O.; Piao, N.; Xia, J.; Pollard, T.; Hou, S.; Zhang, J.; Ji, X.; Xu, J.; Zhang, X.; Ma, L.; He, X.; Liu, S.; Wan, H.; Hu, E.; Zhang, W.; Xu, K.; Yang, X. Q.; Lucht, B.; Wang, C. Enhancing Li^+ transport in NMC811‖graphite lithium-ion batteries at low temperatures by using low-polarity-solvent electrolytes. *Angew. Chem., Int. Ed.* **2022**, *61*, No. e202205967.

(3) Zhang, J.; Zhang, H.; Weng, S.; Li, R.; Lu, D.; Deng, T.; Zhang, S.; Lv, L.; Qi, J.; Xiao, X.; Fan, L.; Geng, S.; Wang, F.; Chen, L.; Noked, M.; Wang, X.; Fan, X. Multifunctional solvent molecule design enables high-voltage Li-ion batteries. *Nat. Commun.* **2023**, *14*, 2211.

(4) Yang, Y. Y. C.; Yin, Y. J.; Davies, D. M.; Zhang, M. H.; Mayer, M.; Zhang, Y. H.; Sablina, E. S.; Wang, S.; Lee, J. Z.; Borodin, O.; Rustomji, C. S.; Meng, Y. S. Liquefied gas electrolytes for wide-temperature lithium metal batteries. *Energy Environ. Sci.* **2020**, *13*, 2209−2219.

(5) Yang, A.; Yang, C.; Xie, K.; Xin, S.; Xiong, Z.; Li, K.; Guo, Y.-G.; You, Y. Benchmarking the safety performance of organic electrolytes for rechargeable lithium batteries: A thermochemical perspective. *ACS Energy Lett.* **2023**, *8*, 836−843.

(6) Wang, Z.; Han, R.; Zhang, H.; Huang, D.; Zhang, F.; Fu, D.; Liu, Y.; Wei, Y.; Song, H.; Shen, Y.; Xu, J.; Zheng, J.; Wu, X.; Li, H. An intrinsically nonflammable electrolyte for prominent-safety lithium metal batteries with high energy density and cycling stability. *Adv. Funct. Mater.* **2023**, *33*, 2215065.

(7) Yu, Z.; Rudnicki, P. E.; Zhang, Z.; Huang, Z.; Celik, H.; Oyakhire, S. T.; Chen, Y.; Kong, X.; Kim, S. C.; Xiao, X.; Wang, H.; Zheng, Y.; Kamat, G. A.; Kim, M. S.; Bent, S. F.; Qin, J.; Cui, Y.; Bao, Z. Rational solvent molecule tuning for high-performance lithium metal battery electrolytes. *Nat. Energy* **2022**, *7*, 94−106.

(8) Suo, L. M.; Hu, Y. S.; Li, H.; Armand, M.; Chen, L. Q. A new class of solvent-in-salt electrolyte for high-energy rechargeable metallic lithium batteries. *Nat. Commun.* **2013**, *4*, 1481.

(9) Wang, J.; Yamada, Y.; Sodeyama, K.; Chiang, C. H.; Tateyama, Y.; Yamada, A. Superconcentrated electrolytes for a high-voltage lithium-ion battery. *Nat. Commun.* **2016**, *7*, 12032.
(10) Ren, X.; Zou, L.; Jiao, S.; Mei, D.; Engelhard, M. H.; Li, Q.; Lee, H.; Niu, C.; Adams, B. D.; Wang, C.; Liu, J.; Zhang, J.-G.; Xu, W. High-concentration ether electrolytes for stable high-voltage lithium metal batteries. *ACS Energy Lett.* **2019**, *4*, 896−902.
(11) Suo, L. M.; Borodin, O.; Sun, W.; Fan, X. L.; Yang, C. Y.; Wang, F.; Gao, T.; Ma, Z. H.; Schroeder, M.; von Cresce, A.; Russell, S. M.; Armand, M.; Angell, A.; Xu, K.; Wang, C. S. Advanced high-voltage aqueous lithium-ion battery enabled by "water-in-bisalt" electrolyte. *Angew. Chem., Int. Ed.* **2016**, *55*, 7136−7141.
(12) Chen, Y. W.; Li, M. H.; Liu, Y.; Jie, Y. L.; Li, W. X.; Huang, F. Y.; Li, X. P.; He, Z. X.; Ren, X. D.; Chen, Y. H.; Meng, X. H.; Cheng, T.; Gu, M.; Jiao, S. H.; Cao, R. G. Origin of dendrite-free lithium deposition in concentrated electrolytes. *Nat. Commun.* **2023**, *14*, 2655.
(13) Jeong, S. K.; Inaba, M.; Iriyama, Y.; Abe, T.; Ogumi, Z. Electrochemical intercalation of lithium ion within graphite from propylene carbonate solutions. *Electrochem. Solid-State Lett.* **2003**, *6*, A13−A15.
(14) Efaw, C. M.; Wu, Q.; Gao, N.; Zhang, Y.; Zhu, H.; Gering, K.; Hurley, M. F.; Xiong, H.; Hu, E.; Cao, X.; Xu, W.; Zhang, J. G.; Dufek, E. J.; Xiao, J.; Yang, X. Q.; Liu, J.; Qi, Y.; Li, B. Localized high-concentration electrolytes get more localized through micelle-like structures. *Nat. Mater.* **2023**, *22*, 1531−1539.
(15) Ren, X.; Chen, S.; Lee, H.; Mei, D.; Engelhard, M. H.; Burton, S. D.; Zhao, W.; Zheng, J.; Li, Q.; Ding, M. S.; Schroeder, M.; Alvarado, J.; Xu, K.; Meng, Y. S.; Liu, J.; Zhang, J.-G.; Xu, W. Localized high-concentration sulfone electrolytes for high-efficiency lithium-metal batteries. *Chem.* **2018**, *4*, 1877−1892.
(16) Li, T.; Zhang, X. Q.; Yao, N.; Yao, Y. X.; Hou, L. P.; Chen, X.; Zhou, M. Y.; Huang, J. Q.; Zhang, Q. Stable anion-derived solid electrolyte interphase in lithium metal batteries. *Angew. Chem., Int. Ed.* **2021**, *60*, 22683−22687.
(17) Chen, J. E.; Zhang, H.; Fang, M. M.; Ke, C. M.; Liu, S.; Wang, J. H. Design of localized high-concentration electrolytes via donor number. *ACS Energy Lett.* **2023**, *8*, 1723−1734.
(18) Chen, K.; Shen, X.; Luo, L.; Chen, H.; Cao, R.; Feng, X.; Chen, W.; Fang, Y.; Cao, Y. Correlating the solvating power of solvents with the strength of ion-dipole interaction in electrolytes of lithium-ion batteries. *Angew. Chem., Int. Ed.* **2023**, *62*, No. e202312373.
(19) Liu, X.; Shen, X.; Luo, L.; Zhong, F.; Ai, X.; Yang, H.; Cao, Y. Designing advanced electrolytes for lithium secondary batteries based on the coordination number rule. *ACS Energy Lett.* **2021**, *6*, 4282−4290.
(20) Zeng, Z.; Murugesan, V.; Han, K. S.; Jiang, X.; Cao, Y.; Xiao, L.; Ai, X.; Yang, H.; Zhang, J.-G.; Sushko, M. L.; Liu, J. Non-flammable electrolytes with high salt-to-solvent ratios for Li-ion and Li-metal batteries. *Nat. Energy* **2018**, *3*, 674−681.
(21) Chen, L.; Wang, J.; Chen, M.; Pan, Z.; Ding, Y.; Song, Z.; Ai, X.; Cao, Y.; Chen, Z. "Dragging effect" induced fast desolvation kinetics and −50 °C workable high-safe lithium batteries. *Energy Storage Mater.* **2024**, *65*, 103098.
(22) Liu, X.; Shen, X.; Li, H.; Li, P.; Luo, L.; Fan, H.; Feng, X.; Chen, W.; Ai, X.; Yang, H.; Cao, Y. Ethylene carbonate-free propylene carbonate-based electrolytes with excellent electrochemical compatibility for Li-ion batteries through engineering electrolyte solvation structure. *Adv. Energy Mater.* **2021**, *11*, 2003905.
(23) Liu, M.; Ma, F.; Ge, Z.; Zeng, Z.; Wu, Q.; Yan, H.; Wu, Y.; Lei, S.; Zhu, Y.; Cheng, S.; Xie, j. In-N-out" design enabling high-content triethyl phosphate-based non-flammable and high-conductivity electrolytes for lithium-ion batteries. *Sci. China Chem.* **2024**, *67*, 724−731.
(24) Qin, M.; Zeng, Z.; Wu, Q.; Yan, H.; Liu, M.; Wu, Y.; Zhang, H.; Lei, S.; Cheng, S.; Xie, J. Dipole-dipole interactions for inhibiting solvent co-intercalation into a graphite anode to extend the horizon of electrolyte design. *Energy Environ. Sci.* **2023**, *16*, 546−556.
(25) Qin, M.; Zeng, Z.; Liu, X.; Wu, Y.; He, R.; Zhong, W.; Cheng, S.; Xie, J. Revealing surfactant effect of trifluoromethylbenzene in medium-concentrated PC electrolyte for advanced lithium-ion batteries. *Adv. Sci.* **2023**, *10*, No. e2206648.
(26) Zhang, H.; Zeng, Z.; He, R.; Wu, Y.; Hu, W.; Lei, S.; Liu, M.; Cheng, S.; Xie, J. 1,3,5-Trifluorobenzene and fluorobenzene co-assisted electrolyte with thermodynamic and interfacial stabilities for high-voltage lithium metal battery. *Energy Storage Mater.* **2022**, *48*, 393−402.
(27) Cheng, H.; Sun, Q.; Li, L.; Zou, Y.; Wang, Y.; Cai, T.; Zhao, F.; Liu, G.; Ma, Z.; Wahyudi, W.; Li, Q.; Ming, J. Emerging era of electrolyte solvation structure and interfacial model in batteries. *ACS Energy Lett.* **2022**, *7*, 490−513.
(28) Ma, M.; Chen, B.; Yang, X.; Liu, Y.; Dai, S.; Qi, X.; Hu, Y.-S.; Pan, H. Solvent reorganization and additives synergistically enable high-performance Na-ion batteries. *ACS Energy Lett.* **2023**, *8*, 477−485.
(29) Peng, X.; Wang, T.; Liu, B.; Li, Y.; Zhao, T. A solvent molecule reconstruction strategy enabling a high-voltage ether-based electrolyte. *Energy Environ. Sci.* **2022**, *15*, 5350−5361.
(30) Zhao, Y.; Zhou, T. H.; Mensi, M.; Choi, J. W.; Coskun, A. Electrolyte engineering via ether solvent fluorination for developing stable non-aqueous lithium metal batteries. *Nat. Commun.* **2023**, *14*, 299.
(31) Liu, S.; Mao, J.; Zhang, L.; Pang, W. K.; Du, A.; Guo, Z. Manipulating the solvation structure of nonflammable electrolyte and interface to enable unprecedented stability of graphite anodes beyond 2 years for safe potassium-ion batteries. *Adv. Mater.* **2021**, *33*, No. e2006313.
(32) Shi, P.; Zheng, H.; Liang, X.; Sun, Y.; Cheng, S.; Chen, C.; Xiang, H. A highly concentrated phosphate-based electrolyte for high-safety rechargeable lithium batteries. *Chem. Commun.* **2018**, *54*, 4453−4456.
(33) Wang, X.; Yasukawa, E.; Kasuya, S. Nonflammable trimethyl phosphate solvent-containing electrolytes for lithium-ion batteries: I. Fundamental properties. *J. Electrochem. Soc.* **2001**, *148*, A1058−A1065.
(34) Suo, L.; Borodin, O.; Gao, T.; Olguin, M.; Ho, J.; Fan, X.; Luo, C.; Wang, C.; Xu, K. Water-in-salt" electrolyte enables high-voltage aqueous lithium-ion chemistries. *Science* **2015**, *350*, 938−943.
(35) Qin, M.; Liu, M.; Zeng, Z.; Wu, Q.; Wu, Y.; Zhang, H.; Lei, S.; Cheng, S.; Xie, J. Rejuvenating propylene carbonate-based electrolyte through nonsolvating interactions for wide-temperature Li-ions batteries. *Adv. Energy Mater.* **2022**, *12*, 2201801.
(36) Huang, Y. Q.; Li, R. H.; Weng, S. T.; Zhang, H. K.; Zhu, C. N.; Lu, D.; Sun, C. C.; Huang, X. T.; Deng, T.; Fan, L. W.; Chen, L. X.; Wang, X. F.; Fan, X. L. Eco-friendly electrolytes *via* a robust bond design for high-energy Li metal batteries. *Energy Environ. Sci.* **2022**, *15*, 4349−4361.
(37) Ma, M.; Chen, B.; Pan, H. Three-dimensional heterogeneity in liquid electrolyte structures promotes Na ion transport and storage performance in Na-ion batteries. *Chem. Sci.* **2023**, *14*, 5983−5991.
(38) Wu, Y.; Hu, Q.; Liang, H.; Wang, A.; Xu, H.; Wang, L.; He, X. Electrostatic potential as solvent descriptor to enable rational electrolyte design for lithium batteries. *Adv. Energy Mater.* **2023**, *13*, 2300259.
(39) Liang, H.; Ma, Z.; Wang, Y.; Zhao, F.; Cao, Z.; Cavallo, L.; Li, Q.; Ming, J. Solvent-solvent interaction mediated lithium-ion (de)intercalation chemistry in propylene carbonate based electrolytes for lithium-sulfur batteries. *ACS Nano* **2023**, *17*, 18062−18073.
(40) van Ekeren, W. W. A.; Albuquerque, M.; Ek, G.; Mogensen, R.; Brant, W. R.; Costa, L. T.; Brandell, D.; Younesi, R. A comparative analysis of the influence of hydrofluoroethers as diluents on solvation structure and electrochemical performance in non-flammable electrolytes. *J. Mater. Chem. A* **2023**, *11*, 4111−4125.
(41) Jia, H.; Xu, Y.; Zhang, X.; Burton, S. D.; Gao, P.; Matthews, B. E.; Engelhard, M. H.; Han, K. S.; Zhong, L.; Wang, C.; Xu, W. Advanced low-flammable electrolytes for stable operation of high-

voltage lithium-ion batteries. *Angew. Chem., Int. Ed.* **2021**, *60*, 12999−13006.

(42) Jia, M.; Zhang, C.; Guo, Y.; Peng, L.; Zhang, X.; Qian, W.; Zhang, L.; Zhang, S. Advanced nonflammable localized high-concentration electrolyte for high energy density lithium battery. *Energy Environ. Mater.* **2022**, *5*, 1294−1302.

https://doi.org/10.1021/jacsau.4c00196
JACS Au 2024, 4, 1986−1996